Natural Fe-bearing aluminous bridgmanite in the Katol L6 chondrite

Sujoy Ghosh[a,1], Kishan Tiwari[a], Masaaki Miyahara[b], Arno Rohrbach[c], Christian Vollmer[c], Vincenzo Stagno[d], Eiji Ohtani[e], and Dwijesh Ray[f]

[a]Department of Geology and Geophysics, Indian Institute of Technology Kharagpur, Kharagpur 721302, India; [b]Graduate School of Advanced Science and Engineering, Hiroshima University, Hiroshima 739-8526, Japan; [c]Institut für Mineralogie, Westfälische Wilhelms-Universität Münster, 48149 Münster, Germany; [d]Department of Earth Sciences, Sapienza University of Rome, Rome 00185, Italy; [e]Department of Earth and Planetary Materials Science, Graduate School of Sciences, Tohoku University, Sendai 980-8578, Japan; and [f]Planetary Sciences Division, Physical Research Laboratory, Ahmedabad 380009, India

Edited by Russell J. Hemley, University of Illinois Chicago, Chicago, IL, and approved August 25, 2021 (received for review May 12, 2021)

Bridgmanite, the most abundant mineral of the Earth's lower mantle, has been reported in only a few shocked chondritic meteorites; however, the compositions of these instances differ from that expected in the terrestrial bridgmanite. Here, we report the first natural occurrence of Fe-bearing aluminous bridgmanite in shock-induced melt veins within the Katol L6 chondrite with a composition that closely matches those synthesized in high-pressure and temperature experiments over the last three decades. The Katol bridgmanite coexists with majorite and metal-sulfide intergrowths. We found that the natural Fe-bearing aluminous bridgmanite in the Katol L6 chondrite has a significantly higher $Fe^{3+}/\Sigma Fe$ ratio (0.69 ± 0.08) than coexisting majorite (0.37 ± 0.10), which agrees with experimental studies. The Katol bridgmanite is arguably the closest natural analog for the bridgmanite composition expected to be present in the Earth's lower mantle. Textural observations and comparison with laboratory experiments suggest that the Katol bridgmanite formed at pressures of ∼23 to 25 gigapascals directly from the chondritic melt generated by the shock event. Thus, the Katol L6 sample may also serve as a unique analog for crystallization of bridgmanite during the final stages of magma ocean crystallization during Earth's formation.

bridgmanite | chondrite | magma ocean | oxygen fugacity | lower mantle

Bridgmanite is a dominant phase in the Earth's lower mantle (1, 2) where it constitutes about 75 wt% of peridotitic composition (3) and is stable from 660- to 2,700-km depth. The crystal structure of natural bridgmanite with the unit formula $(Mg_{0.75}Fe_{0.20}Na_{0.03}Ca_{0.02}Mn_{0.01})SiO_3$ has been reported for the first time in the shock-melt veins of the Tenham L6 chondrite (4). The fine-grained polycrystalline bridgmanite in the Tenham L6 chondrite is formed by solid-state phase transformation from orthoenstatite and contains almost no Al_2O_3 (close to 0.2 wt%) (4, 5). More recently, Bindi et al. (6) reported the discovery of a Fe-rich analog of bridgmanite (hiroseite) in the Suizhou L6 chondrite with a composition $(Fe^{2+}_{0.44}Mg_{0.37}Fe^{3+}_{0.10}Al_{0.04}Ca_{0.03}Na_{0.02})(Si_{0.89}Al_{0.11})O_3$ containing 6.5 wt% Al_2O_3. Although these findings in natural materials may resemble the mineralogy of the Earth's lower mantle, their chemical compositions differ significantly from those produced experimentally (7, 8). High-pressure experimental studies provide evidence that bridgmanite takes up most of the Al_2O_3 (9) of the mantle and contains up to 5 wt% of Al_2O_3 in a peridotitic bulk composition (10–12). The few natural occurrences of bridgmanite-like inclusions in superdeep diamonds contain variable amounts of Al_2O_3 ranging from less than 2 to 13 wt% (13–15). However, these inclusions represent the residue of back-transformation reactions occurred during the ascent of kimberlite magma from the deep mantle to the surface. The variation of Al content in bridgmanite has been explained in light of two substitution mechanisms for the incorporation of Al^{3+} into bridgmanite (16).

The first coupled substitution is represented as follows:

$$Al^{3+}(VI) + Al^{3+}(VIII) \leftrightarrow Si^{4+}(VI) + Mg^{2+}(VIII), \quad [1]$$

where aluminum enters both cation sites and corresponds to the exchange vector $[Al^{(VI)}Al^{(VIII)}][Si^{(VI)}Mg^{(VIII)}]_{-1}$. Italic numbers in parentheses indicate the coordination number of the respective cation.

The second mechanism is described as follows:

$$2Al^{3+}(VI) + V^0(O^-) \leftrightarrow 2Si^{4+}(VI) + O^{2-}, \quad [2]$$

where aluminum replaces silicon and oxygen vacancies provide charge balance (V^0 indicates vacancy) corresponding to the exchange vector $[Al_2^{(VI)}V^0][Si_2^{(VI)}O]_{-1}$. Reaction 1 is the energetically most favorable coupled substitution mechanism (e.g., 17).

Furthermore, the observed linear dependence between Al and Fe^{3+} in synthetic bridgmanite has been explained by a coupled substitution (7, 8, 18) corresponding to the exchange vector $[Mg^{(VIII)}Si^{(VI)}][Fe^{3+(VIII)}Al^{(VI)}]_{-1}$:

$$Mg^{2+}(VIII) + Si^{4+}(VI) \leftrightarrow Fe^{3+}(VIII) + Al^{3+}(VI). \quad [3]$$

High-pressure experiments supported by natural observations suggest that bridgmanite shows $Fe^{3+}/\Sigma Fe$ ratios higher than 0.6 at lower-mantle P-T conditions and low oxygen fugacity (fo_2),

Significance

Bridgmanite is the most volumetrically abundant mineral of the Earth's interior, and it is important to understand its formation mechanism to better comprehend the origin and evolution of planetary interiors. Natural bridgmanites have been reported in only a few shocked meteorites; however, the composition of these specimens differs from plausible compositions of terrestrial bridgmanite. This study reports a natural occurrence of bridgmanite, observed in an ordinary chondrite, with a composition closest to the bridgmanite present in the Earth's lower mantle. The bridgmanite in the Katol chondrite has high $Fe^{3+}/\Sigma Fe$ ratio and agrees with experimental predictions. The Katol chondrite may serve as a unique analogue for crystallization of bridgmanite during the final stages of magma ocean crystallization of the Earth.

Author contributions: S.G. designed research; K.T., M.M., A.R., C.V., and D.R. analyzed data; S.G. and K.T. wrote the paper; and V.S. and E.O. interpreted collected data.

The authors declare no competing interest.

This article is a PNAS Direct Submission.

[1]To whom correspondence may be addressed. Email: sujoy.ghosh@gg.iitkgp.ac.in.

This article contains supporting information online at https://www.pnas.org/lookup/suppl/doi:10.1073/pnas.2108736118/-/DCSupplemental.

Published September 29, 2021.

which is significantly higher than what exhibited by upper mantle silicate minerals at low fo_2 (19, 20). Here, we report the first natural occurrence of Fe-bearing aluminous bridgmanite and discuss its formation mechanisms through the analyses of coexisting majorite and metal–sulfide intergrowths in the Katol L6 chondrite. We propose that Fe-bearing aluminous bridgmanite from Katol was crystallized at pressures of 23 to 25 GPa from the chondritic melt generated by the shock event. We also measured $Fe^{3+}/\Sigma Fe$ of natural bridgmanite and majorite formed by shock metamorphism. Our results reveal that Fe-bearing aluminous bridgmanite has a higher $Fe^{3+}/\Sigma Fe$ than coexisting majorite and confirm the experimental observations of high Fe^{3+} content in bridgmanite at lower-mantle conditions.

Results

The Katol meteorite is an L6 ordinary chondrite fallen near the town of Katol in the Nagpur district of India after a large meteor shower occurred on May 22, 2012 (21, 22). The host rock is mainly composed of olivine (Fo_{75}), low-Ca pyroxene ($En_{75}Fs_{22}Wo_3$), high-Ca pyroxene ($En_{46}Fs_{10}Wo_{44}$), albitic plagioclase ($Ab_{84}An_{11}Or_5$), which has been partly converted into a glass (maskelynite), plus chromite, apatite, Fe-Ni metal, and troilite as accessory phases (*SI Appendix*, Table S1). The host rock shows a network of abundant shock-melt veins (veins are 75 μm to 1,200 μm wide; *SI Appendix*, Fig. S1), enclosing rounded fragments of host minerals in a fine-grained matrix.

The shock-melt veins exhibit two different lithologies showing distinctive textures: coarse-grained fragments entrained in the veins embedded in a fine-grained matrix (Fig. 1*A*). The coarse-grained fragments are compositionally identical to the host rock material. The chondritic fragments in the shock-melt veins include mostly fractured, rounded, coarse, polycrystalline grains of wadsleyite, ringwoodite, majorite, akimotoite, lingunite, and tuite (*SI Appendix*, Figs. S2–S4 and Table S1). Furthermore, the matrix portion of the shock-melt vein consists of two different phase assemblages showing distinct textures. In the inner portion of a shock melt vein, the fine-grained matrix consists of euhedral and rounded grains (1 to 5 μm) of majorite–pyrope solid solution (Maj-Prp_{ss}) and metal–sulfide eutectic intergrowths (Fig. 1*B*). Raman spectroscopic analyses show characteristic vibrational bands of Maj-Prp_{ss} at 350, 588, 656, and 929 cm^{-1} (*SI Appendix*, Fig. S5). Metal–sulfide eutectic intergrowths fill the interstices between Maj-Prp_{ss} grains.

The outer portion of the fine-grained matrix (0.5- to 5-μm diameter grains) near the host rock–vein boundary (i.e., vein edge) mainly consists of submicron-sized grains of partially vitrified bridgmanite coexisting with majorite and iron–nickel–sulfide intergrowths (Fig. 1*C*). Bridgmanite crystals range from about 100 to 1,000 nm in their longest dimension and show granular and idiomorphic morphologies (Fig. 2*A*), which is completely different from bridgmanites reported from previous studies (4, 6). The selected-area electron diffraction (SAED) pattern of the dark phase in the center of the glass can be indexed to orthorhombic bridgmanite with unit-cell parameters of $a = 5.10$ Å, $b = 6.93$ Å, $c = 4.81$ Å, a cell volume of 170 $Å^3$ and space group *Pnma* (Fig. 2 *B* and *C*). The observed unit-cell volume of the Katol bridgmanite is larger than that reported for pure $MgSiO_3$ (V =162.3 $Å^3$; 23–24), (Mg, Fe^{2+})SiO_3 bridgmanite (V =162.8 to 163.2 $Å^3$; 23–26) and Al-free bridgmanite (V = 167 $Å^3$) found in a shock-melt vein of the Tenham L6 chondrite (4) and is similar to hiroseite (V = 169.7 $Å^3$) discovered in a shock-melt vein of the Suizhou L6 chondrite (6). Scanning transmission electron microscopy–energy-dispersive spectroscopy (STEM-EDS) analyses of the Fe-bearing aluminous bridgmanite yield a chemical formula of $(Mg_{0.74(10)}Fe_{0.13(5)}Al_{0.05(1)}Ca_{0.02(1)}Na_{0.02(2)})(Si_{0.95(4)}Al_{0.05(1)})O_3$. The value in parentheses is the SD of the calculation. Fe-bearing aluminous bridgmanite from the Katol L6 chondrite has high Al_2O_3 content (~4.8 ± 0.3 wt%), low FeO content (~8.9 ± 3.0 wt%),

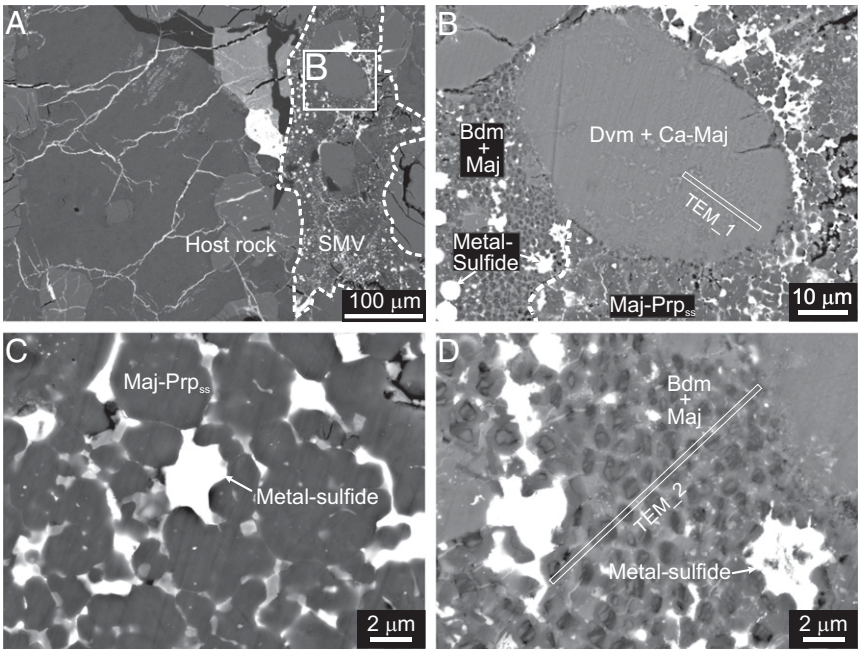

Fig. 1. Back-scattered electron images of the Katol L6 chondrite: (*A*) Portion of the sample shows shock-melt vein with various rounded fragments in the host rock entrained in a finer matrix. The host rock is distinguished from the shock-melt vein by a dashed line. Scale bars, 100 μm. (*B*) The phase assemblages in the shock-melt vein matrix of the Katol L6 chondrite can be divided into two groups marked by a dashed line. An elliptical-shaped chondritic fragment of 60 × 40 μm size along its axes entrained in the center part of the shock-melt vein has been transformed to vitrified davemaoite (Dvm) glass and subcalcic majorite (Ca-Maj). Scale bars, 10 μm. (*C*) High-magnification image of the right-hand side vein portion of the dashed line shows euhedral and rounded to subhedral grains of majorite-pyrope solid solution (Maj-Prp_{ss}) coexisting with metal-sulfide intergrowth. Scale bars, 2 μm. (*D*) High-magnification image of the left-hand side vein portion of the dashed line shows submicron-sized euhedral grains of Fe-bearing aluminous bridgmanite (Bdm) coexists with majorite (Maj) and metal-sulfide blebs. Scale bars, 2 μm.

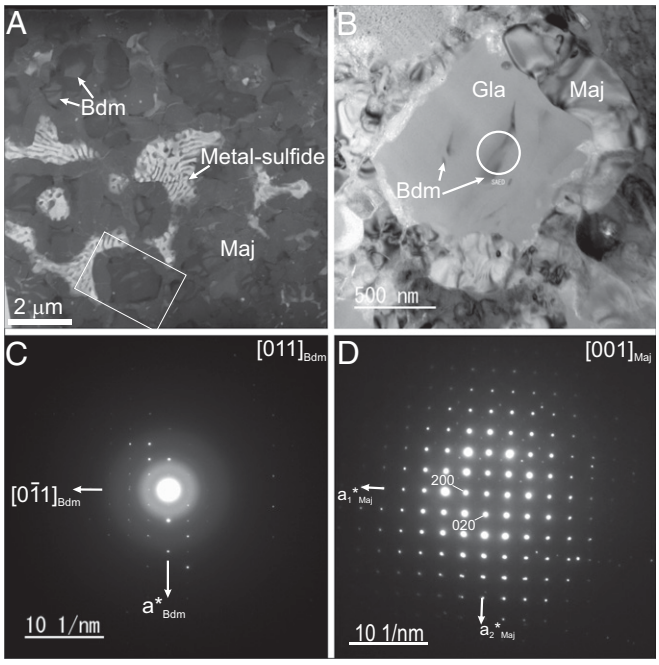

Fig. 2. TEM images show Fe-bearing aluminous bridgmanite, majorite, and FeNi-FeS melt in the Katol L6 chondrite: (*A*) High-angle annular dark-field (HAADF) image of an aggregate of submicrometer-sized crystals of bridgmanite enclosed in vitrified bridgmanite glass within a shock-melt vein from the Katol L6 chondrite. Majorite is found in the vein matrix together with a small metal-sulfide melt. The rectangle mark (TEM_2) shows where the TEM lamella was prepared by FIB. Scale bars, 2 μm. (*B*) BF (Bright-field)-TEM image of high magnification FE-SEM in backscattered electron (BSE) mode of Fe-bearing aluminous bridgmanite coexisting with majorite and Fe-Ni-sulfide intergrowths. Euhedral grains present in the center are partially vitrified bridgmanite with crystalline bridgmanite preserved in the center of the grain, whereas majorite occupies the interspaces. Electron diffraction patterns from the circled area are shown in Fig. 3C. Scale bars, 500 μm. (*C*) The SAED patterns of bridgmanite along the [011] zone axis. This diffraction pattern can be only indexed by orthorhombic bridgmanite with space group *Pnma*. Scale bars, 10 1/nm. (*D*) The SAED pattern of Maj along the [001] zone axis. Scale bars, 10 1/nm.

low Na_2O content (0.7 ± 0.6 wt%), and similar MgO (28.8 ± 4.4 wt%) and CaO contents (1.1 ± 0.5 wt%) compared with previously reported Al-free bridgmanite from the Tenham L6 chondrite (4) (Table 1). The majorite coexisting with Fe-bearing aluminous bridgmanite [Mg# = molar Mg/(Mg+Fe^{total}) × 100 of 71; Table 1] has lattice parameters of a = 12.08 Å and V = 1,763 $Å^3$, therefore slightly larger than synthetic majorite with an Mg# of 79 (a = 11.52 Å, V = 1,528.8 $Å^3$; 27) and natural majorite from meteorites with Mg# of 71 to 75 (a = 11.51 Å, V = 1,524.8 $Å^3$; 28, 29). This discrepancy is mainly attributed to uncertainties in the values of lattice parameters determined by TEM and differences in the chemical composition such as iron content. EDS analysis gives a bulk stoichiometric composition for majorite from the Katol L6 chondrite as $(Mg_{1.87}Fe^{2+}_{0.57}Na_{0.30}Ca_{0.27})(Si_{1.0}\ Mg_{0.29}Fe^{3+}_{0.33}Al_{0.27}Cr_{0.07}Ti_{0.04})(SiO_4)_3$ (Table 1). Several rounded, coarse-grained diopside fragments (40 to 60 μm) entrained at the center of the shock-melt vein have transformed to submicron-sized rounded and euhedral grains of vitrified davemaoite (30) coexisting with relatively large subhedral grains of subcalcic majorite (Ca-majorite; Fig. 3 *A* and *B*). EDS analysis of vitrified davemaoite and Ca-majorite grains, obtained by TEM, gives the composition as $(Ca_{0.52}Mg_{0.36}Fe_{0.08}Cr_{0.08}Al_{0.01})(Si_{0.98}Al_{0.02})O_3$ and $Ca_{0.66}Mg_{2.48}Fe_{0.54}Cr_{0.21}Al_{0.1}Si_{4.01}O_{12}$, respectively.

The $Fe^{3+}/\Sigma Fe$ ratios of Fe-bearing aluminous bridgmanite and majorite in the Katol L6 chondrite were measured using electron energy loss spectroscopy (EELS) and are reported in Table 1 (*SI Appendix*, Figs. S8 and S9). The $Fe^{3+}/\Sigma Fe$ ratio of Fe-bearing aluminous bridgmanite from Katol varies from 0.53 to 0.97 and shows generally higher values than coexisting majorite which varies from 0.29 to 0.48.

Discussion

Impact-induced formation of bridgmanite has been reported previously in shocked meteorites (for example, Acfer 040, Tenham, Suizhou, and DaG 735) (4–6, 31–33). Bridgmanite crystals in the Tenham L6 chondrite consist of fine-grained polycrystalline aggregates and are always associated with akimotoite. Moreover, bridgmanite from the Tenham L6 chondrite contains almost no aluminum and has an Mg# of 87. The bridgmanite from the Tenham L6 chondrite was interpreted to form by a solid-state phase transformation from orthoenstatite. Hiroseite from the Suizhou L6 chondrite was found to coexist with ferropericlase and ringwoodite/ahrensite solid solution that confirm the high-pressure (and temperature) origin of hiroseite that likely formed by the solid-state transformation from pristine Fe-rich olivine. In contrast, the idiomorphic, microcrystalline texture and aluminum enrichment relative to the host low-Ca pyroxene, as shown by EDS analysis, indicates that the Fe-bearing aluminous bridgmanites present in the matrix of shock-melt veins in the Katol L6 chondrite are the liquidus phase and have crystallized from a chondritic melt at high pressure by homogeneous nucleation. The chemical composition of bridgmanite is consistent with bridgmanite fractionated during a magma ocean event as predicted from high-pressure experiments (8). Crystallization starts at the vein–host rock boundary and moves toward the center of the vein. Maj-Prp_{ss} probably formed in the inner portion of the vein as a result of small-pressure change during crystallization. The difference in texture and grain size between these two assemblages is probably due to rapid quenching along the vein edge. It is interesting to note that a similar texture has been observed in the Tenham L6 chondrite by Xie et al. (31).

The rounded shape of $CaSiO_3$ plus Ca-majorite fragment suggests that it may have experienced marginal melting in this part of the melt vein (Fig. 3*A*). SAED patterns of $CaSiO_3$ glass show diffuse diffraction spots, which may indicate vitrification of davemaoite due to pressure release (Fig. 3*C*). The approximate bulk composition of the fragment ($En_{49}Fs_{11}Wo_{40}$) is similar to the host diopside ($En_{46}Fs_{10}Wo_{41}$), which suggests that Ca-majorite and vitrified davemaoite are dissociation products of diopside and may have formed by a solid-state reaction (Table 1). The majorite coexisting with Fe-bearing aluminous bridgmanite in the vein matrix portion contains ~3.1 ± 0.3 wt% Al_2O_3 whereas the Ca-majorite coexisting with the $CaSiO_3$ glass in the fragment have lower Al_2O_3 contents (1.1 ± 0.3 wt%), which further consolidate the possibility that vitrified davemaoite and Ca-majorite are dissociated products of diopside and did not crystallize from the chondritic melt. Similar phase assemblages have been reported previously in the Y-75100 H6 chondrite (34). Furthermore, Raman spectroscopic analyses show characteristic bands of Ca-majorite (24) at 357, 590, 644, and 924 cm^{-1} and davemaoite (35, 36) at 649 and 966 cm^{-1}, respectively (*SI Appendix*, Fig. S6). We estimated the pressure for Ca-rich majorite using the machine-learning geobarometer of Thomson et al. (37) that yields pressure of 18.5 ± 0.2 GPa. This pressure calculation is consistent with phase relations in $CaMgSi_2O_6$ system (37) that suggest diopside dissociates into majorite and davemaoite in the pressure range of 18 to 22 GPa.

Melting experiments on peridotitic and chondritic compositions (38–41) have shown that bridgmanite is the liquidus phase at ~25 GPa. Textural and compositional evidence indicate that Fe-bearing aluminous bridgmanite in the Katol L6 chondrite is of similar origin and crystallized from the chondritic melt generated by the shock event. Phase relations studies in a pyrolite composition show that aluminum solubility in bridgmanite coexisting with majorite below 24 GPa increases from 3.7 to 4.9 wt% to

Table 1. Chemical composition of Fe-bearing aluminous bridgmanite (Mg, Fe, and Al-Bdm), majorite (Maj), and associated phases (davemaoite: Dvm; Ca-majorite: Ca-Maj) in the Katol L6 chondrite and previously reported bridgmanite (Bdm) coexisting with akimotoite in the Tenham L6 chondrite and hiroseite (Hir) in the Suizhou L6 chondrite (values in atomic per formula unit)

Phase	Location	*n*	Si	Ti	Cr	Al	Fe*	Mg	Ca	Na	Total	Mg/(Mg+Fe)	Ca/(Ca+Mg+Fe)	$Fe^{3+}/\Sigma Fe$
Mg, Fe, Al-Bdm	Katol†	5	0.948 (0.04)	0.007 (0.01)	0.004 (0.01)	0.098 (0.01)	0.128 (0.05)	0.741 (0.10)	0.020 (0.01)	0.023 (0.02)	1.971	0.85	0.02	0.69 (0.08)
Maj	Katol†	4	3.996 (0.29)	0.038 (0.03)	0.068 (0.06)	0.269 (0.02)	0.898 (0.36)	2.159 (0.64)	0.267 (0.02)	0.302 (0.15)	8.000	0.71	0.08	0.37 (0.10)
Dvm	Katol†	10	0.977 (0.01)	—	0.077 (0.04)	0.024 (0.01)	0.075 (0.01)	0.355 (0.02)	0.523 (0.03)	—	1.992	0.83	0.55	
Ca-Maj	Katol†	4	4.012 (0.02)	—	0.208 (0.02)	0.095 (0.02)	0.543 (0.02)	2.479 (0.05)	0.664 (0.04)	—	8.000	0.82	0.18	
Bdm	Tenham (4)	7	0.990	0.003	0.002	0.004	0.204	0.741	0.017	0.031	1.991	0.78	0.02	0.20‡
Hir	Suizhou (6)	3	0.890	bd	0	0.150	0.540	0.370	0.020	0.030	2.000	0.41	0.02	0.19

Numbers given inside parentheses are one SD of the mean based on the number of analyses. *n* = number of analyses.
*Total Fe as Fe^{2+}.
†This study.
‡The ferric iron content of Tenham bridgmanite is calculated by stoichiometry from electron probe data.

~7.0 wt% with majorite breakdown at ~25 GPa in peridotitic mantle (42). The Al_2O_3 content of bridgmanite present in the Katol L6 chondrite matches well with experimental data on carbonaceous chondrite and peridotitic compositions and suggests that bridgmanite would be the major reservoir of aluminum at lower mantle conditions. Moreover, shocked meteorites mostly contain vitrified bridgmanite, mainly because the postshock temperature of the shock-melt veins is generally higher than the thermal stability limit of bridgmanite at lower pressure resulting in vitrification of the bridgmanite during the pressure release. However, Tschauner et al. (4) reported crystalline bridgmanite in the Tenham L6 chondrite and attributed its existence to induced stress in the surrounding rock owing to volume expansion of ~33% upon the transformation of bridgmanite into $MgSiO_3$-glass. Pressure–temperature conditions for the formation of bridgmanite in the Katol L6 chondrite have been estimated by experimental data on chondritic meteorites (38–40) (*SI Appendix*, Fig. S7). Experimental studies on the Allende carbonaceous chondrite have shown that the liquidus phase changes from majorite to bridgmanite at about 25 GPa (40), whereas the experimentally derived low-pressure stability limit of bridgmanite in a pyrolitic composition is 23 GPa (42). We additionally estimated the formation pressure for the majorite coexisting with Fe-bearing aluminous bridgmanite at the vein margin of Katol chondrite using majorite geobarometer (37). This geobarometer indicates that the majorite formed at a pressure of ~19.8 GPa ± 0.7 GPa, which is in good agreement with the estimated crystallization pressure obtained using the liquidus phase assemblages (23 to 25 GPa). Thus, the phase assemblages present in shock-melt veins in the Katol L6 chondrite effectively imply an origin of Katol L6 at pressures of about 23 to 25 GPa, whereas the estimated temperature is ~2,323 K (i.e., the predicted liquidus temperature of Allende meteorite at that pressure) (*SI Appendix*, Fig. S7). The formation and subsequent preservation of high-pressure phases present in the shock-melt veins is mainly a function of rapid crystallization of the melt vein before the onset of decompression. Therefore, the presence of high-pressure phases implies that the crystallization time was shorter than the duration of the shock pulse, which does not allow such high-pressure phases to decompose into more stable low-pressure phases. The cooling history of different meteorites has been previously modeled (43) and has been used to constrain the cooling time of shock-melt veins to subsolidus temperature (29, 44). The model indicates that a shock-melt vein about 1 mm-thick would require about 1 s to cool down to subsolidus. A similar thickness (1.2 mm) of shock-melt vein in the Katol L6 chondrite would have quenched on the order of ~1 s and suggests that the shock pulse must have persisted for at least 1 s. This estimation of shock pulse duration is in agreement with previously reported values (31, 45–47).

Based on high-pressure experiments, it has been argued that bridgmanite has a $Fe^{3+}/\Sigma Fe$ ratio of more than 0.5 but less than 0.7 when coexisting with metallic Fe under lower mantle conditions, which makes the oxygen fugacity (fo_2) of the primordial lower mantle reduced [$\log fo_2$ < iron-wüstite (*IW*) buffer] and buffered by 1 wt% metallic Fe-Ni alloy (8). On the other hand,

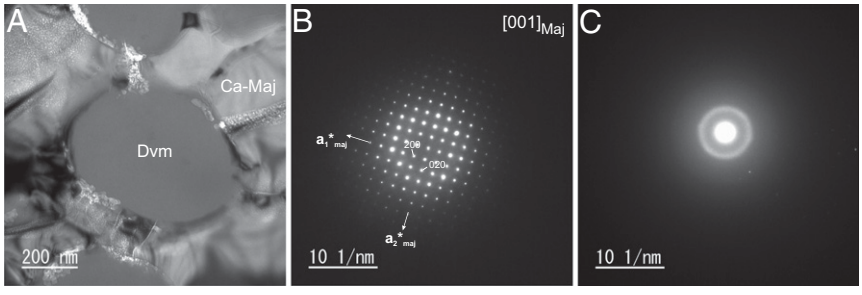

Fig. 3. TEM images show vitrified davemaoite (Dvm), subcalcic majorite (Ca-Maj) in the Katol L6 chondrite: (*A*) Bright-field (BF)-TEM image of submicron-sized rounded and euhedral grains of vitrified davemaoite coexisting with relatively larger subhedral to euhedral grains of Ca-Maj in the chondritic fragment entrained in the shock-melt vein. The rectangle on the right side of Fig. 1*A* (TEM_1) shows the location of TEM lamella prepared by FIB. Scale bars, 200 nm. (*B*) The SAED patterns of Ca-Maj along the [001] zone axis. Scale bars, 10 1/nm. (*C*) The SAED pattern of davemaoite shows diffuse diffraction spots, that indicates vitrification of davemaoite possibly due to the pressure release. Scale bars, 10 1/nm.

bridgmanite coexisting with diamond and carbonate (solid/melt) [log$fo_2 \sim IW+2$] can have a $Fe^{3+}/\Sigma Fe$ up to 0.8 (48). Fe-bearing aluminous bridgmanites from the Katol L6 chondrite do show high $Fe^{3+}/\Sigma Fe$ contents consistent with synthetic bridgmanite with a similar chemical composition quenched from high P-T experiments. Although the effect of local fo_2 in the $Fe^{3+}/\Sigma Fe$ of bridgmanite is still debated, no evidence of Fe(Ni) metal alloys were found within the shock vein hosting high-pressure phases in the Katol L6 chondrite. There is evidence that metallic Fe coexisting with hiroseite was recently reported from the Suizhou L6 chondrite (6) and linked to disproportionation reactions as $3Fe^{2+} = Fe^0 + 2Fe^{3+}$. In the case of Suizhou chondrite, hiroseite was less oxidized, hence containing only $Fe^{3+}/\Sigma Fe$ of 0.12 that is significantly lower than the present bridgmanite. Therefore, we cannot exclude that the crystallization of Fe-bearing aluminous bridgmanite in the Katol meteorite might have occurred under oxidizing conditions. This conclusion is further supported by the observation that subcalcic majorite inclusions [Ca# of 0.16 (0.04)] in diamonds with $Fe^{3+}/\Sigma Fe$ of about 0.4 equilibrated with oxidized mantle fluids (49). Fe^{3+} contents of Fe-bearing aluminous bridgmanite and majorite in the shock-metamorphosed meteorite are in good agreement with those reported from high-pressure experiments (8, 48, 50). There are no experimental data, however, for partitioning of Fe^{3+} between bridgmanite and majorite.

Microanalyses of the Fe-bearing aluminous bridgmanite of the Katol L6 chondrite reveal that Si^{4+} is deficient (0.95 apfu) in the smaller octahedral B site; therefore, some amounts of Al^{3+} (0.05 apfu) would compensate for Si in the B site, while the larger A site is occupied by the remaining Al^{3+} (0.05 apfu) along with trivalent (Fe^{3+}), divalent (Mg, Fe^{2+}, Ca), and monovalent (Na) cations. EELS and STEM-EDS data further help to refine the chemical formula of bridgmanite as $(Mg_{0.74}Fe^{3+}_{0.09}Al_{0.05}Fe^{2+}_{0.04}Ca_{0.02}Na_{0.02})(Si_{0.95}Al_{0.05})O_3$. Synthetic and natural bridgmanites show a significant increase in the unit-cell volume with incorporation of Fe^{3+} into the bridgmanite structure (Fig. 4) (51, 52). For example, the unit-cell volume increases from 163.1 $Å^3$ at ~0.03 apfu Fe^{3+} to 169 $Å^3$ at 0.38 apfu Fe^{3+} in synthetic bridgmanite (51, 52). As there are no Fe^{3+} concentration data available on bridgmanite from Tenham (4), we calculated the Fe^{3+} content in bridgmanite from stoichiometry to see the relationship between unit-cell volume and Fe^{3+} content in natural bridgmanites (4, 6) and compare this value with Fe-bearing aluminous bridgmanite from this study. We noticed that the slope of natural bridgmanite is steeper than that of synthetic bridgmanite suggesting that unit-cell volume of the natural bridgmanites is more sensitive to incorporation of trivalent cations (Fe and/or Al) in the bridgmanite structure. Additionally, the higher estimated temperature of formation of bridgmanite in shocked meteorites can be an additional factor that is responsible for the observed larger volume in natural bridgmanites. Furthermore, it has been suggested that the ferric iron content in aluminous bridgmanite is positively correlated with aluminum content, whereas aluminum-free bridgmanite contains distinctly less ferric iron (7, 18). Aluminum-free bridgmanite from the Tenham L6 chondrite shows high concentrations of Na (0.9 wt%) and advocates Na-Fe^{3+} coupled substitution in these bridgmanites (4). However, Fe-bearing aluminous bridgmanite from the Katol L6 chondrite encompasses low concentrations of Na and supports $Fe^{3+} + Al^{3+}$ as a primary coupled substitution mechanism in bridgmanite at fo_2 above the *IW* buffer. Also, bridgmanite formed by shock metamorphism shows a similar chemical composition and ferric iron content to those reported from high-pressure experiments, which suggests equilibrium conditions in the shock-melt veins of the Katol L6 chondrite. The natural Fe-bearing aluminous bridgmanite from the Katol L6 chondrite observed in this study with high Fe_2O_3 concentration has important implications for the evolution of the redox state of the Earth's deep mantle. The Moon-forming giant impact hypothesis suggests that the Earth should have melted to a depth of 750 to 1,100 km and formed a deep magma ocean (53, 54). The Katol bridgmanite richer in ferric than ferrous iron coexisting with metal sulfide melt may serve as analog for crystallization from an oxidizing silicate magma coexisting with iron sulfide melt. These conditions may have existed on Earth during the last stage of the magma ocean in the early history of Earth when sulfide melts segregated at slightly higher fo_2 than that of the *IW* buffer and can be a natural simulation of the "Hadean matte" hypothesis (55).

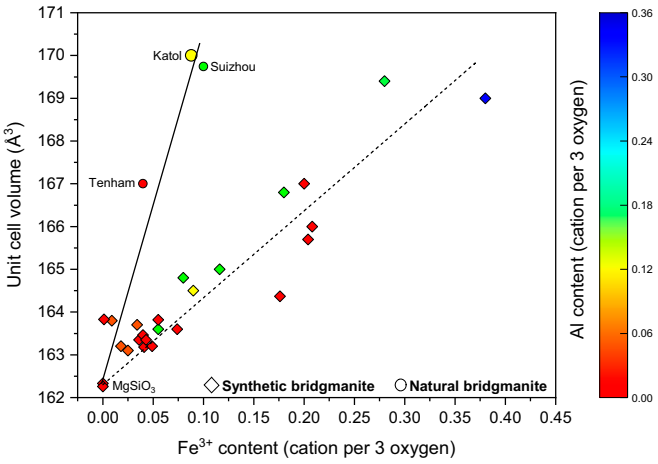

Fig. 4. Unit-cell volume of bridgmanite as a function of Fe^{3+} and Al contents of synthetic and natural bridgmanite. Filled circles: Natural bridgmanite (Katol: This study; Tenham: 4; Suizhou: 6); Filled diamonds: Synthetic bridgmanite (50, 51). The ferric iron content of Tenham bridgmanite is calculated by stoichiometry from electron probe data.

Materials and Methods

A chunk sample of the Katol L6 chondrite was embedded in epoxy resin, ground, and polished using 3-μm followed by 1-μm and 0.25-μm diamond paste.

Scanning Electron Microscopy. A JEOL JSM-6490 scanning electron microscope (SEM) equipped with an EDS installed at Indian Institute of Technology (IIT) Kharagpur was used for textural observations and phase identification at an accelerating voltage of 15 kV.

Field Emission Scanning Electron Microscopy. We employed a field emission scanning electron microscopy (FE-SEM), Zeiss Supra 40, and JEOL JSM-7000F, operating at an accelerating voltage of 15 kV at Central Research Facility, IIT Kharagpur and Department of Earth and Planetary Materials Science, Tohoku University for fine textural observations.

Electron Microprobe. Major element compositions of the phases were determined with a CAMECA SX100 electron microprobe at the Planetary Sciences Division, Physical Research Laboratory, operated at 20 nA and 15 kV, and calibrated against silicate, sulfide, and metal standards (21). All data were converted to oxide concentrations using a Pouchou and Pichoir reduction scheme.

Micro-Raman Spectrometer. The mineralogy of the samples was determined using a laser micro-Raman spectrometer, Horiba Jobin Yvon LabRam HR800 with a liquid nitrogen-cooled charge coupled device (CCD) detector at Department of Physics, Indian Institute of Science Education and Research, Kolkata. A microscope (objective: X 10) was used to focus the excitation laser beam (a He-Ne laser, 633-nm line with 1,800 L /mm grating). Laser power on a sample was kept at 7.5 mW to hinder material damage. Acquisition times were 10 to 30 s. For each phase, a Raman shift was acquired in the spectral region of 200 to 1,200 cm^{-1}. A few phases were also determined using a laser micro-Raman and a JASCO NRS-2000 spectrometer with a liquid nitrogen–cooled CCD detector at Department of Earth Sciences, Tohoku University. A microscope was used to focus the excitation laser beam (the 487.99-nm lines of a Princeton Instruments Ar laser). The laser power on the sample was kept at 7.5 mW to hinder material damage.

Transmitted Electron Microscopy. A slice for transmitted electron microscopy (TEM) observations was prepared by a focused ion beam (FIB) system: JEOL 9320-FIB at Tohoku University. A gallium ion beam was accelerated to 30 kV during the sputtering of the slices, and the slices were ~100 nm in thickness. A JEOL JEM-2100F FE-TEM operating at 200 kV with a JEOL EDS detector system was used for conventional TEM observation and SAED analysis at Tohoku University. We determined the chemical composition of each mineral by STEM mode with the EDS detector and an average collection time of 2 to 3 s. The chemical compositions were corrected using the experimentally determined *k*-factors, and *k*-factors for major elements were determined using the standards for albite, pyrope, almandine, San Carlos olivine, and synthetic (Mg,Fe)O.

Electron Energy-Loss Spectroscopy. $Fe^{3+}/\Sigma Fe$ ratios of bridgmanite and majorite were investigated at University of Münster with a Zeiss Libra 200 FE transmission electron microscope operated at 200 kV, equipped with an in-column Omega energy filter. The energy resolution of acquired energy loss spectra was about 0.7 eV, measured at the full width at half-maximum of the zero-loss peak. Molar $Fe^{3+}/\Sigma Fe$ ratios were obtained at the Fe-$L_{2,3}$ absorption edges at around 708 to 721 eV using the EELSA MatLab script (56) based on the quantification routines by van Aken and Liebscher (57) and van Aken et al. (58).

Data Availability. All study data are included in the article and/or *SI Appendix*.

ACKNOWLEDGMENTS. We thank C.A. McCammon and N. Rai for valuable discussion and A. Thomson for comments on the revised version of the manuscript. S.G. acknowledges financial support by Council of Scientific and Industrial Research Grant No. 24(0362)/20/EMR-II.

1. A. E. Ringwood, Phase transformations and their bearing on the constitution and dynamics of the mantle. *Geochim. Cosmochim. Acta* **55**, 2083–2110 (1991).
2. M. Murakami, K. Hirose, K. Kawamura, N. Sata, Y. Ohishi, Post-perovskite phase transition in $MgSiO_3$. *Science* **304**, 855–858 (2004).
3. L. Stixrude, C. Lithgow-Bertelloni, Geophysics of chemical heterogeneity in the mantle. *Annu. Rev. Earth Planet. Sci.* **40**, 569–595 (2012).
4. O. Tschauner *et al*., Mineralogy. Discovery of bridgmanite, the most abundant mineral in Earth, in a shocked meteorite. *Science* **346**, 1100–1102 (2014).
5. N. Tomioka, K. Fujino, Natural $(Mg,Fe)SiO_3$-ilmenite and -perovskite in the Tenham meteorite. *Science* **277**, 1084–1086 (1997).
6. L. Bindi, S. H. Shim, T. G. Sharp, X. Xie, Evidence for the charge disproportionation of iron in extraterrestrial bridgmanite. *Sci. Adv.* **6**, eaay7893 (2020).
7. B. J. Wood, D. C. Rubie, The effect of alumina on phase transformations at the 660-kilometer discontinuity from Fe-Mg partitioning experiments. *Science* **273**, 1522–1524 (1996).
8. D. J. Frost *et al*., Experimental evidence for the existence of iron-rich metal in the Earth's lower mantle. *Nature* **428**, 409–412 (2004).
9. W. F. McDonough, S. S. Sun, The composition of the Earth. *Chem. Geol.* **120**, 223–253 (1995).
10. J. Zhang, D. J. Weidner, Thermal equation of state of aluminum-enriched silicate perovskite. *Science* **284**, 782–784 (1999).
11. B. J. Wood, Phase transformations and partitioning relations in peridotite under lower mantle conditions. *Earth Planet. Sci. Lett.* **174**, 341–354 (2000).
12. D. J. Frost, F. Langenhorst, The effect of Al_2O_3 on Fe–Mg partitioning between magnesiowüstite and magnesium silicate perovskite. *Earth Planet. Sci. Lett.* **199**, 227–241 (2002).
13. T. Stachel, J. W. Harris, G. P. Brey, W. Joswig, Kankan diamonds (Guinea) II: Lower mantle inclusion parageneses. *Contrib. Mineral. Petrol.* **140**, 16–27 (2000).
14. C. McCammon, H. Mark, H. Jeff, Ferric iron content of mineral inclusions in diamonds from Sao Luiz: A view into the lower mantle. *Science* **278**, 434–436 (1997).
15. F. Kaminsky, Mineralogy of the lower mantle: A review of 'super-deep'mineral inclusions in diamond. *Earth Sci. Rev.* **110**, 127–147 (2012).
16. A. Navrotsky, A lesson from ceramics. *Science* **284**, 1788–1789 (1999).
17. S. Akber-Knutson, M. S. Bukowinski, The energetics of aluminum solubility into $MgSiO_3$ perovskite at lower mantle conditions. *Earth Planet. Sci. Lett.* **220**, 317–330 (2004).
18. C. McCammon, Perovskite as a possible sink for ferric iron in the lower mantle. *Nature* **387**, 694–696 (1997).
19. H. S. C. O'Neill *et al*., "Ferric iron in the upper mantle and in transition zone assemblages: Implications for relative oxygen fugacities in the mantle" in *Evolution of the Earth and Planets*, E. Takahashi, R. Jeanloz, D. Rubie, Eds. (American Geophysical Union/International Union of Geodesy and Geophysics Geophysical Monograph, 1993). pp. 73–88.
20. D. Canil, H. S. C. O'Neill, Distribution of ferric iron in some upper-mantle assemblages. *J. Petrol.* **37**, 609–635 (1996).
21. G. Suresh *et al*., Katol meteorite shower, Maharashtra: A preliminary study. *J. Geol. Soc. India* **81**, 151–157 (2013).
22. D. Ray, S. Ghosh, S. V. S. Murty, On the possible origin of troilite-metal nodules in the Katol chondrite (L6-7). *Meteorit. Planet. Sci.* **52**, 72–88 (2017).
23. Y. Wang, D. J. Weidner, R. C. Liebermann, Y. Zhao, P–V–T equation of state of (Mg,Fe)SiO_3 perovskite: Constraints on composition of the lower mantle. *Phys. Earth Planet. Inter.* **83**, 13–40 (1994).
24. S. Lundin *et al*., Effect of Fe on the equation of state of mantle silicate perovskite over 1 Mbar. *Phys. Earth Planet. Inter.* **168**, 97–102 (2008).
25. Y. Fei, D. Virgo, B. O. Mysen, Y. Wang, H. K. Mao, Temperature-dependent electron delocalization in $(Mg,Fe)SiO_3$ perovskite. *Am. Mineral.* **79**, 826–837 (1994).
26. J. B. Parise, Y. Wang, A. Yeganeh-Haeri, D. E. Cox, Y. Fei, Crystal structure and thermal expansion of $(Mg,Fe)SiO_3$ perovskite. *Geophys. Res. Lett.* **17**, 2089–2092 (1990).
27. S. V. Sinogeikin, J. D. Bass, A. Kavner, R. Jeanloz, Elasticity of natural majorite and ringwoodite from the Catherwood meteorite. *Geophys. Res. Lett.* **24**, 3265–3268 (1997).
28. R. Jeanloz, Majorite: Vibrational and compressional properties of a high-pressure phase. *J. Geophys. Res.* **86**, 6171–6179 (1981).
29. J. Hu, T. G. Sharp, High-pressure phases in shock-induced melt of the unique highly shocked LL 6 chondrite Northwest Africa 757. *Meteorit. Planet. Sci.* **51**, 1353–1369 (2016).
30. O. Tschauner, S. Huang, S. Yang, M. Humayun, Davemaoite. *Min. Mag.* **84**, 975 (2020).
31. Z. Xie, T. G. Sharp, P. S. DeCarli, High-pressure phases in a shock-induced melt vein of the Tenham L6 chondrite: Constraints on shock pressure and duration. *Geochim. Cosmochim. Acta* **70**, 504–515 (2006).
32. T. G. Sharp, C. M. Lingemann, C. Dupas, D. Stöffler, Natural occurrence of $MgSiO_3$-ilmenite and evidence for $MgSiO_3$-perovskite in a shocked L chondrite. *Science* **277**, 352–355 (1997).
33. M. Miyahara *et al*., Natural dissociation of olivine to $(Mg,Fe)SiO_3$ perovskite and magnesiowustite in a shocked Martian meteorite. *Proc. Natl. Acad. Sci. U.S.A.* **108**, 5999–6003 (2011).
34. N. Tomioka, M. Kimura, The breakdown of diopside to Ca-rich majorite and glass in a shocked H chondrite. *Earth Planet. Sci. Lett.* **208**, 271–278 (2003).
35. J. D. Kubicki, R. J. Hemley, A. M. Hofmeister, Raman and infrared study of pressure-induced structural changes in $MgSiO_3$, $CaMgSi_2O_6$, and $CaSiO_3$ glasses. *Am. Mineral.* **77**, 258–269 (1992).
36. C. D. Yin, M. Okuno, H. Morikawa, F. Marumo, T. Yamanaka, Structural analysis of $CaSiO_3$ glass by X-ray diffraction and Raman spectroscopy. *J. Non-Cryst. Solids* **80**, 167–174 (1986).
37. A. R. Thomson, S. C. Kohn, A. Prabhu, M. J. Walter, Evaluating the formation pressure of diamond-hosted majoritic garnets: A machine learning majorite barometer. *J. Geophys. Res. Solid Earth* **126**, e2020JB020604 (2021).
38. C. B. Agee, J. Li, M. C. Shannon, S. Circone, Pressure temperature phase diagram for the Allende meteorite. *J. Geophys. Res. B Solid Earth* **100**, 17725–17740 (1995).
39. M. Chen, A. El Goresy, D. Frost, P. Gillet, Melting experiments of a chondritic meteorite between 16 and 25 GPa: Implication for Na/K fractionation in a primitive chondritic Earth's mantle. *Eur. J. Mineral.* **16**, 203–211 (2004).
40. Y. Asahara, T. Kubo, T. Kondo, Phase relations of a carbonaceous chondrite at lower mantle conditions. *Phys. Earth Planet. Inter.* **143–144**, 421–432 (2004).
41. E. Ito, E. Takahashi, Melting of peridotite at uppermost lower-mantle conditions. *Nature* **328**, 514–517 (1987).
42. T. Ishii, H. Kojitani, M. Akaogi, Phase relations and mineral chemistry in pyrolitic mantle at 1600–2200° C under pressures up to the uppermost lower mantle: Phase transitions around the 660-km discontinuity and dynamics of upwelling hot plumes. *Phys. Earth Planet. Inter.* **274**, 127–137 (2018).
43. C. S. Shaw, E. Walton, Thermal modeling of shock melts in Martian meteorites: Implications for preserving Martian atmospheric signatures and crystallization of high-pressure minerals from shock melts. *Meteorit. Planet. Sci.* **48**, 758–770 (2013).
44. E. L. Walton, T. G. Sharp, J. Hu, J. Filiberto, Heterogeneous mineral assemblages in Martian meteorite Tissint as a result of a recent small impact event on Mars. *Geochim. Cosmochim. Acta* **140**, 334–348 (2014).
45. E. Ohtani *et al*., Formation of high-pressure minerals in shocked L6 chondrite Yamato 791384: Constraints on shock conditions and parent body size. *Earth Planet. Sci. Lett.* **227**, 505–515 (2004).
46. M. Miyahara, E. Ohtani, A. Yamaguchi, Albite dissociation reaction in the Northwest Africa 8275 shocked LL chondrite and implications for its impact history. *Geochim. Cosmochim. Acta* **217**, 320–333 (2017).
47. I. Baziotis *et al*., High pressure minerals in the Château-Renard (L6) ordinary chondrite: Implications for collisions on its parent body. *Sci. Rep.* **8**, 9851 (2018).
48. V. Stagno *et al*., The stability of magnesite in the transition zone and the lower mantle as function of oxygen fugacity. *Geophys. Res. Lett.* **38**, 19 (2011).
49. E. S. Kiseeva *et al*., Oxidized iron in garnets from the mantle transition zone. *Nat. Geosci.* **11**, 144 (2018).
50. A. Rohrbach *et al*., Metal saturation in the upper mantle. *Nature* **449**, 456–458 (2007).
51. D. R. Hummer, Y. Fei, Synthesis and crystal chemistry of Fe3+-bearing (Mg, Fe^{3+})(Si, Fe^{3+})O_3 perovskite. *Am. Min.* **97**, 1915–1921 (2012).
52. R. Sinmyo *et al*., Effect of Fe^{3+} on phase relations in the lower mantle: Implications for redox melting in stagnant slabs. *J. Geophys. Res. Solid Earth* **124**, 12484–12497 (2019).
53. B. J. Wood, M. J. Walter, J. Wade, Accretion of the Earth and segregation of its core. *Nature* **441**, 825–833 (2006).
54. J. Wade, B. J. Wood, Core formation and the oxidation state of the Earth. *Earth Planet. Sci. Lett.* **236**, 78–95 (2005).
55. H. S. C. O'Neill, The origin of the Moon and the early history of the Earth-A chemical model. Part 2: The Earth. *Geochim. Cosmochim. Acta* **55**, 1159–1172 (1991).
56. C. Prescher, F. Langenhorst, L. S. Dubrovinsk, V. B. Prakapenka, N. Miyajima, The effect of Fe spin crossovers on its partitioning behavior and oxidation state in a pyrolitic Earth's lower mantle system. *Earth Planet. Sci. Lett.* **399**, 86–91 (2014).
57. P. A. van Aken, B. Liebscher, Quantification of ferrous/ferric ratios in minerals: New evaluation schemes of Fe L_{23} electron energy-loss near-edge spectra. *Phys. Chem. Miner.* **29**, 188–200 (2002).
58. P. A. van Aken, B. Liebscher, V. J. Styrsa, Quantitative determination of iron oxidation states in minerals using Fe $L_{2,3}$-edge electron energy-loss near-edge structure spectroscopy. *Phys. Chem. Miner.* **25**, 323–327 (1998).